

Konferenz: 25.02.03

Konferenzband: Juni 2003

## Compaction and Rarefaction of Fused Silica with 193-nm Excimer Laser Exposure

J. Martin Algots<sup>a</sup>, Richard Sandstrom<sup>a</sup>, William Partlo<sup>a</sup>, Petar Maroevic<sup>a</sup>,  
Eric Eva<sup>b</sup>, Michael Gerhard<sup>b</sup>, Ralf Lindner<sup>b</sup>, Frank Stietz<sup>b</sup>

<sup>a</sup>Cymer, Inc., 16750 Via del Campo Ct, San Diego, CA, USA 92127;

<sup>b</sup>Carl Zeiss Semiconductor Manufacturing Technologies AG, 73446 Oberkochen, Germany

### ABSTRACT

Extensive testing of the 193 nm laser damage behavior of fused silica has been performed over the past few years by several researchers. The results have shown that compaction and rarefaction / expansion of the material can occur. The actually observed process depends on the studied fused silica type, the used energy density, and laser pulse number at constant pulse length. In order to check the influence of the different laser parameters in more detail, an experimental set up has been constructed that allows us to investigate not only the influence of the energy density and laser pulse number but also the effect of the integrated square pulse width on the laser damage behavior. An optical delay line is used to create a longer integrated pulse width than the natural laser pulse width. To make these tests relevant to the microlithography community, the integrated energy densities chosen for these tests span the range typically found in the projection optics of a 193 nm excimer laser-based microlithography tool. The samples are exposed to several billions of pulses with wavefront measurements made periodically.

**Keywords:** Lithography, Excimer, ArF, Fused Silica, Compaction, Rarefaction, Pulse Stretch.

### 1. INTRODUCTION

During the last several years, strong improvements of the quality of fused silica have been realized making this material more suitable for the use in 193 nm microlithography. One of the major concerns related to the use of fused silica is the damage that the material suffers during exposure to 193 nm radiation. Upon exposure it can physically and optically compact (compaction or densification) and it can physically and optically expand (de-compaction or rarefaction)<sup>1</sup>. Compaction results in an increase of the optical index of refraction and in a shortening of the geometrical length of the sample in the irradiated area. As the influence of the index change is much larger than the change in dimensions, the overall effect is one of retarded wavefront. Rarefaction is just the opposite effect, i.e. resulting in an accelerated wavefront. Because the changes in sample dimensions are small, the laser induced wavefront change  $\Delta(n \cdot L)/L$  normalized to sample length  $L$  is approximately the same as the index change  $\Delta n$ . In this paper, we will make no difference between the normalized wavefront change and the index change.

The actually observed process and in particular its absolute amount depend on the studied fused silica material as well as the applied laser energy density and number of laser pulses. Thus, the ability to model the changes in optical index of refraction as a function of the above mentioned parameters are on the one hand important to further improve the fused silica material and on the other hand needed to effectively design a modern lithography lens. The excimer lasers used to illuminate a 193 nm lithographic tool are pulsed lasers, with pulse lengths on the order of 20 nsec. The effect of the pulse length of the lasers has now become a variable in the lens design due to the use of pulse stretching technology by the laser manufacturers. As a consequence, the influence of this parameter on laser damage of fused silica has to be studied.

---

\* malgots@cymer.com; phone 858/385-5241

This paper discusses a test of the effect of energy density and pulse length on the laser induced changes of the optical index of refraction of fused silica induced by 193 nm irradiation. A model will be provided that predicts the changes as a function of energy density and pulse duration.

## 2. TEST SET UP

### 2.1. Laser configuration

The laser used for this experiment was a Cymer Nanolith 7000 (NL7000). A standard production NL7000 laser is rated at 5 mJ, 4000 Hz, 75% duty cycle. The laser used for this test was highly modified to allow it to run at higher pulse energies and to run at 4000 Hz, 100% duty cycle. The modifications included the removal of external panels, the use of additional fans, and the use of some prototype modules to help dissipate the extra heat generated by the high duty cycle operation and higher energies.

The laser cavity was built with partial reflectors of 30% on both ends, providing broadband radiation (see Figure 1).

Apertures on both ends of the cavity were 2.6(w) x 12.5(h) mm. Bandwidth is estimated at 0.5 nm FWHM from measurements of other ArF broadband systems. Radiation is produced from both ends of the cavity through the 30% reflectors. The radiation from the left end of the cavity travels through a two-prism anamorphic beam expander (expanding the width 4x) and is then routed with mirrors to the optical table. This beam is referred to as

the non-stretched beam. The radiation from the right side of the cavity goes through a second anamorphic beam expander (4x), through an optical pulse stretcher, and then on to the optical table, parallel to the non-stretched beam. This beam from the right side of the cavity is referred to as the stretched beam.

The optical pulse stretcher is a re-imaging time delay loop consisting of a beam splitter and four concave mirrors creating a confocal resonator. The delay is 22 nsec and the overall efficiency is approximately 85-90%. Typical stretched and non-stretched temporal profiles are shown in Figure 2.

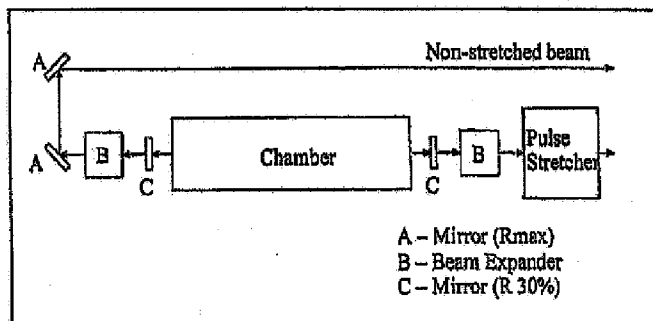


Figure 1 - Laser Configuration

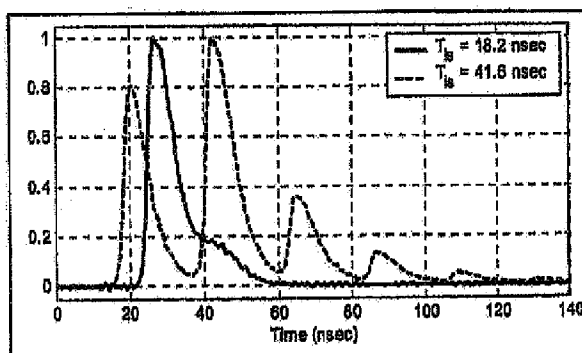


Figure 2 - Typical Normalized Pulse Shape

### 2.2. Test configuration

The experiment was run on a 12 x 4 foot optical table covered with a custom aluminum enclosure with glass windows. The enclosure is purged with nitrogen and oxygen levels are measured and maintained below 10 ppm.

Both stretched and non-stretched beams enter the table and are individually rotated 90° with mirrors giving a beam size of 6mm high x 13 mm wide. The polarization of each beam is rotated with ¼ wave plates and then expanded horizontally with a pair of prisms to produce 6 mm x 22 mm beams. Each stretched and non-stretched beam is then split into 3 parallel beams to illuminate three sets of samples. The optics are designed to pass the non-stretched beams parallel to, and 10 mm above, the corresponding stretched beam (see Figure 3).

The energy of each stretched and non-stretched beam can be controlled with their own counter-rotating plate attenuators. The beams are then split and attenuated with 3 parallel plate attenuators to deliver four beams each one  $\frac{1}{2}$  the energy density of the previous (see section 2.3 Exposure Protocol). Finally the beams pass through an aperture plate to provide a clean beam shape and a quartz  $\frac{1}{4}$  waveplate to induce rotational polarization.

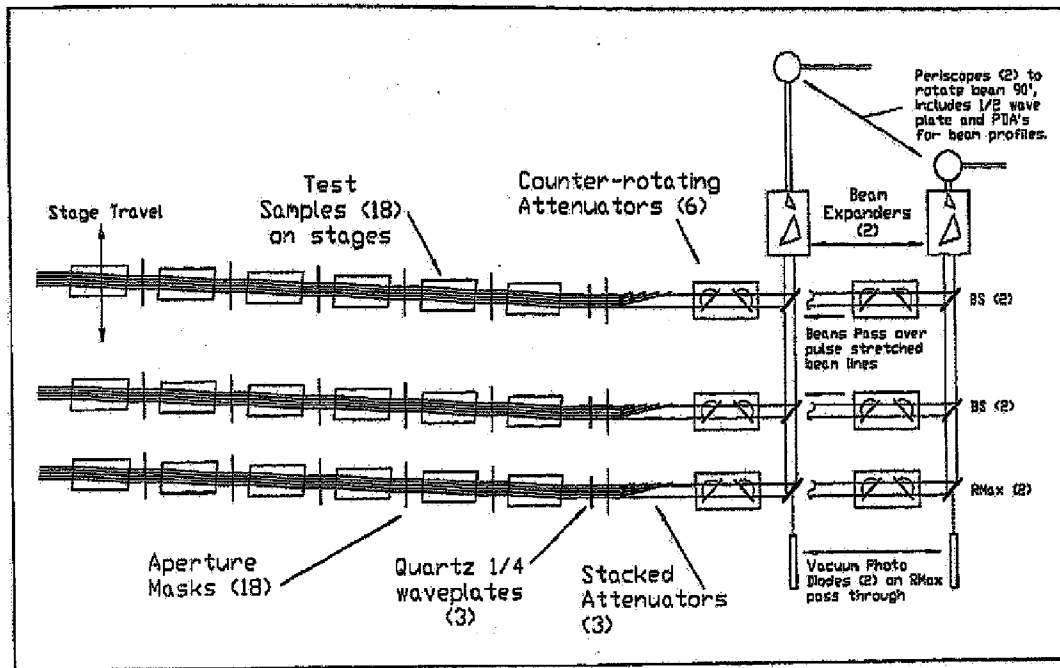


Figure 3 - Optics Table Layout

Each of the three beam lines illuminates 6 samples in series, single pass. The samples are mounted on translation stages, such that they can be moved in and out (perpendicular to) the beams. Behind each of the first five samples in each beam line is an additional aperture, of the same geometry as the first, which cleans up the beam before it reaches the next sample. These inter-sample apertures are on computer-controlled actuators that allow the apertures to be flipped out of the beam path during the insitu measurement process.

### 2.3. Exposure Protocol

The samples measured 60 mm wide x 30 mm high x 100 mm long. The samples were exposed through the 100 mm length. Each sample was exposed with eight beams, two rows of four beams each (see Figure 4). The four top beams were from the non-stretched side of the laser and the four bottom beams were from the stretched. Each beam delivered  $\frac{1}{2}$  as much pulse energy as the previous, so that nominal energy densities of 100, 50, 25 and 13  $\mu\text{J}/\text{cm}^2$  were achieved on the same sample at the same time.

With six samples illuminated in series, the Fresnel reflections of each surface reduce the energy density on each downstream sample. To reduce the build up of reflections in the samples, apertures were installed between each sample to clean up the beam and block most of the reflections from samples further down stream.

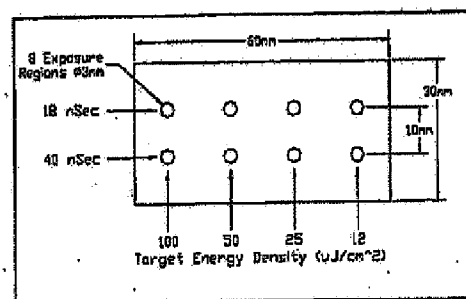


Figure 4 - Illumination of Sample.

#### 2.4. Insitu Metrology

Several parameters were measured during the exposure of the samples. At roughly 15-minute intervals the pulse shapes, pulse counts, and the  $O_2$  level of the enclosure were recorded. The temporal pulse shapes of the stretched and non-stretched beams were measured using Hamamatsu vacuum photo diodes. The pulse shapes were recorded with an oscilloscope and  $t_p$  was computed with a LabView program.

The laser chamber required a gas refill every day. Before and after each refill, an automated measurement routine was performed. This routine consisted of measuring the power and spatial distribution of the beams incident on and transmitted through each sample. A Moletron power head and a 14-bit Lumogen UV coated CCD camera were mounted on an X-Y stage. The stage positioned the power meter and camera before or after each sample, working it's way from the last sample to the first.

Due to the limited aperture of the power meter, it could not capture all eight beams of a sample. Instead, it was positioned to capture the 6 highest energy beams. The camera was then positioned to take three images, each one capturing 4 beams, such that all beams were imaged (the middle four beams were imaged twice).

#### 2.5. Exsitu Metrology

A Zygo 633 nm interferometer was used to measure the effect of the radiation on the samples every 2.5 billion pulses. The interferometer was mounted on a floating optics table and enclosed in an aluminum cover. The set up was dedicated to this test and not changed or modified between measurements.

The samples were held on a fully automated stage that allowed for remote positioning of the samples to record the front surface, back surface and the transmitted wavefront parallel to the exposure volume in the samples. Four images were taken of each surface and in transmission, as well as four reference images with the sample moved out of the field of view.

### 3. Data Analysis

#### 3.1. Interferometry

The final wavefronts were created by averaging the four transmission measurements, and then subtracting the average of the four reference measurements. For the wavefront measured at any given pulse count (i.e. 5 billion), the 0 pulse wavefront was then subtracted. The zero reference subtraction became important to remove the major wavefront curvature inherent in the sample. Figure 5 shows a typical interferogram, taken after 10 billion pulses of exposure. The compacted areas (negative wavefront defect) can be clearly seen. The upper row corresponds to beams 1, 2, and 3 (left - right), and the lower row corresponds to beams 5, 6, and 7 (left - right). One-dimensional slices through the compacted areas are shown in Figure 6.

The background noise level of the interferograms limits the accuracy with which the defect amplitudes can be judged. The effects of noise can be reduced by applying a 'spot-meter' spatial filter which is designed to match the geometry of the compacted spot, while rejecting noise components. This filter consists of a circular region with a diameter 0.75 times the exposing beam diameter, surrounded by a concentric annulus with an inner diameter 1.5 times the beam diameter and outer diameter 2.5 times the beam diameter (see Figure 7). For each point the filter is centered on, the spot-meter reading for that point is equal to the average of the values within the central spot minus the average of the values contained in the annulus. The effect is to average the amplitude within the central region while performing a localized baseline subtraction. Both piston and local tilt in the wavefront are effectively removed. A circular 'top-hat' structure (like the compaction spot) is passed by the filter unattenuated.

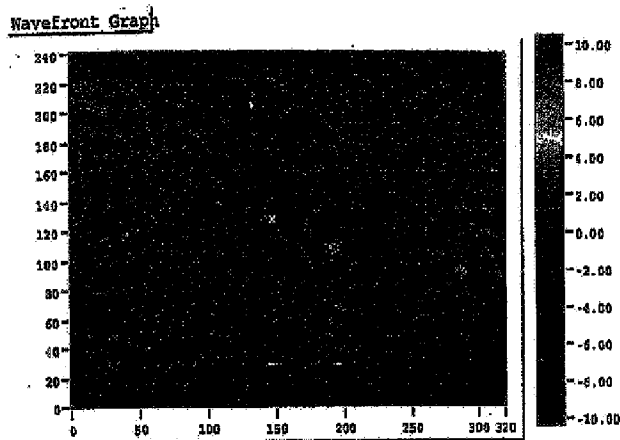


Figure 5 -- Typical interferogram after 10 B shots, 6 exposure regions shown (image in nanometers).

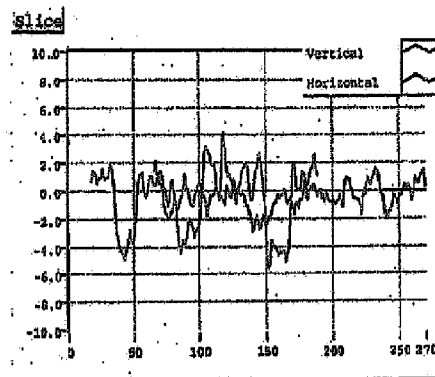


Figure 6 - Cross-section of Figure 5 along cross hairs

A 'spot-metered' version of the interferogram is shown in Figure 8. For every point on the original interferogram, the spot-meter value has been computed. The effectiveness of the spot filter in reducing noise is apparent. Whereas in the original interferogram it is difficult to pick out the compaction defects for beams 3 and 7 (right hand side), they can be clearly seen in the filtered version. Slices through the compacted areas are shown in Figure 9. The height of the compaction spot is taken to be the most positive or negative spot-meter value in the vicinity of the spot (ideally, this occurs when the filter is centered on the compaction spot).



Figure 7 - Spot meter design.

### 3.2. Illumination Calculations

The CCD camera images of the incident radiation were processed for each sample and each measurement to determine the energy density for each exposure spot. The three images from each sample were stitched together and scaled appropriately to produce a single image of all eight beams. The 6 highest intensity beams (those measured by the power meter) of this composite image were integrated and the power reading associated with this image was used to calibrate

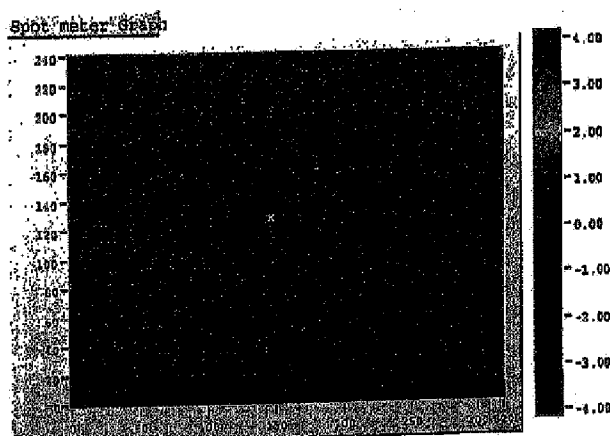


Figure 8 -- Spot meter filtered interferogram of Figure 5 (image in nanometers).

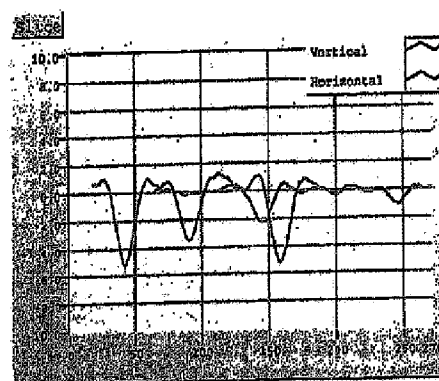


Figure 9 - Cross-section of Figure 8 along cross hair.

the image into energy density (mJ/cm<sup>2</sup>).

#### 4. Results and Model

The results obtained in these experiments show that different types of fused silica can exhibit a wide range of characteristics. Depending on the studied material and applied laser energy density, either compaction or rarefaction are observed.

The results for sample #1, shown in Figure 10, represent a fused silica formulation where compaction is the major contributor to index change. Exposures done with energy densities as low as 0.011 mJ/cm<sup>2</sup> lead to a positive change in

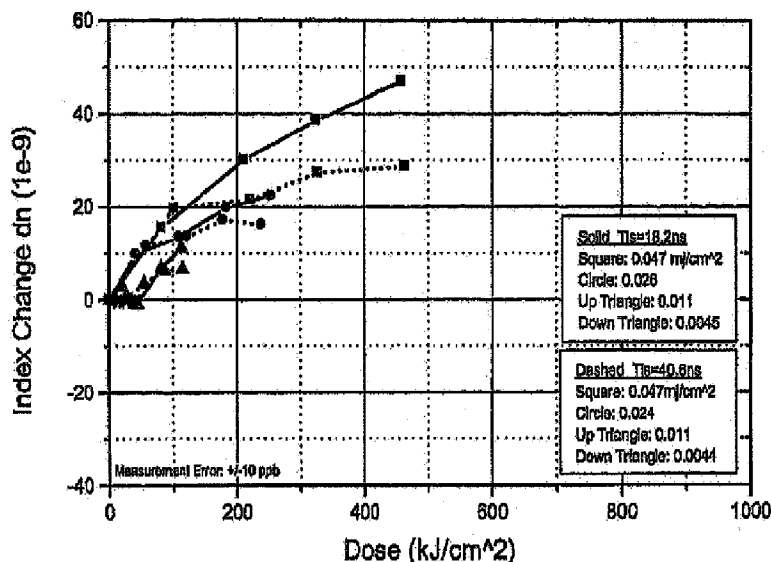


Figure 10 - Measured refractive index change for two laser pulse durations and several different energy densities.

refractive index. Published models for compaction follow the form<sup>3</sup>:

$$\Delta n = \left( k_2 \frac{NI^2}{t_{is}} \right)^b;$$

where  $\Delta n$  is the index change,  $k_2$  is a material dependent constant,  $N$  is the number of pulses,  $I$  is the energy density (mJ/cm<sup>2</sup>) of a single pulse, and  $t_{is}$  is the integral square pulse width (ns) defined by<sup>4</sup>:

$$t_{is} = \frac{\left[ \int T(t) dt \right]^2}{\int T^2(t) dt};$$

where  $T(t)$  is the laser pulse shape in time. Traditionally, the  $k_2$  constant is written outside the parenthesis, but we have chosen to place it inside so that it will have sensible units.

This compaction model predicts that the measured index change when exposed to different values of energy density and pulse duration will follow a single curve when plotted against  $\left(\frac{NI^2}{t_p}\right)$ . Figure 11 shows the data for sample #1 re-plotted with the x-axis appropriately modified. The data points now all fall on a single line regardless of energy density or pulse duration.

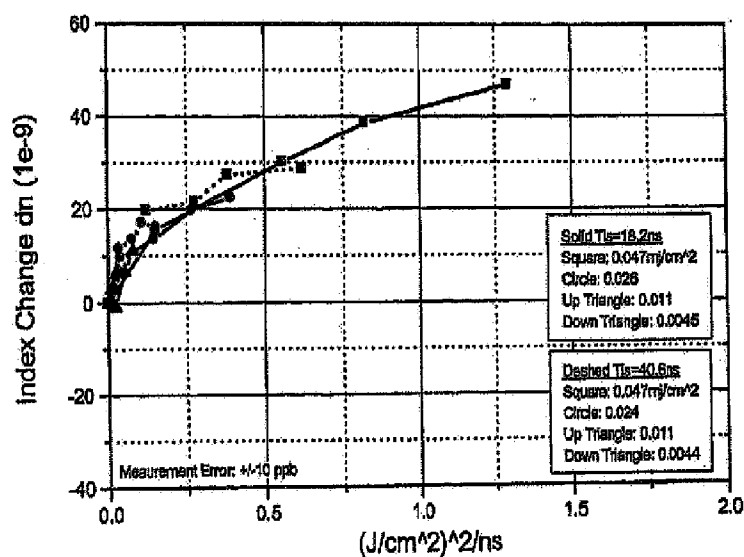


Figure 11 - Measured refractive index change for sample #1 plotted against  $\left(\frac{NI^2}{t_p}\right)$ .

Sample #2 is an example of a material dominated by rarefaction<sup>5</sup>, as shown in Figure 12. For all energy densities tested

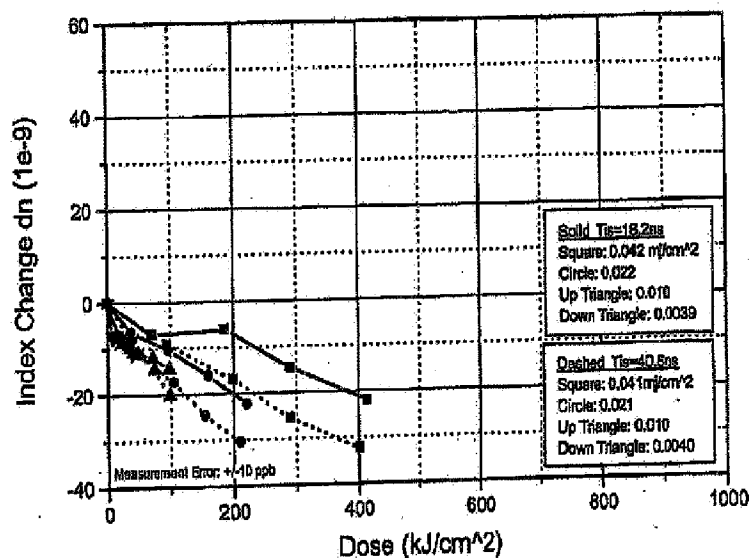


Figure 12 - Measured refractive index change for sample #2, dominated by rarefaction.

in this sample, even as high as  $0.044 \text{ mJ/cm}^2$ , the refractive index change was negative.

Figure 13 shows the data for sample #2 plotted with  $\left(\frac{NI^2}{t_p}\right)$  as the x-axis. Clearly this material does not fit the pure compaction model.

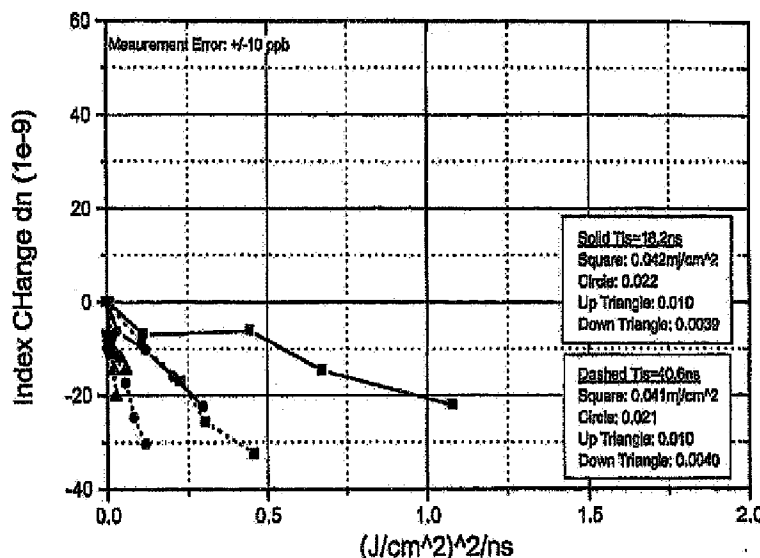


Figure 13 - Measured data for sample #2 plotted against  $\left(\frac{NI^2}{t_p}\right)$ .

The proposed model for rarefaction has a linear dependence on energy density and no dependence on pulse duration<sup>5</sup>. Based on earlier studies, the index change with exposure in the rarefaction model is known to saturate as a function of pulse number and energy density. This rarefaction model can be written as shown below:

$$\Delta n = \Delta n_{sat} \left( 1 - e^{-\frac{NI}{D_0}} \right);$$

where  $\Delta n_{sat}$  is the fully saturated index change and  $D_0$  is the e-folding dose for the rarefaction effect.

As one can see in the measured results for sample #2, there is still some dependence on pulse duration. We infer from this result that the refractive index change is not purely rarefaction, but contains some compaction effects. The positive index change from compaction compensates part of the negative index change induced by rarefaction. Since compaction is reduced with a longer pulse duration, an increase in the total negative index change is observed due to less balancing.

An example of a material with a balance between rarefaction and compaction is sample #3, with its measured results shown in Figure 14. Most notable is the measured index change when exposed at  $0.087 \text{ mJ/cm}^2$  with a  $t_p$  pulse duration of 18.2ns. Under these conditions the index change hovers around  $10 \times 10^{-9}$  out to an accumulated dose of  $870 \text{ kJ/cm}^2$ , or equivalently 10 billion pulses.



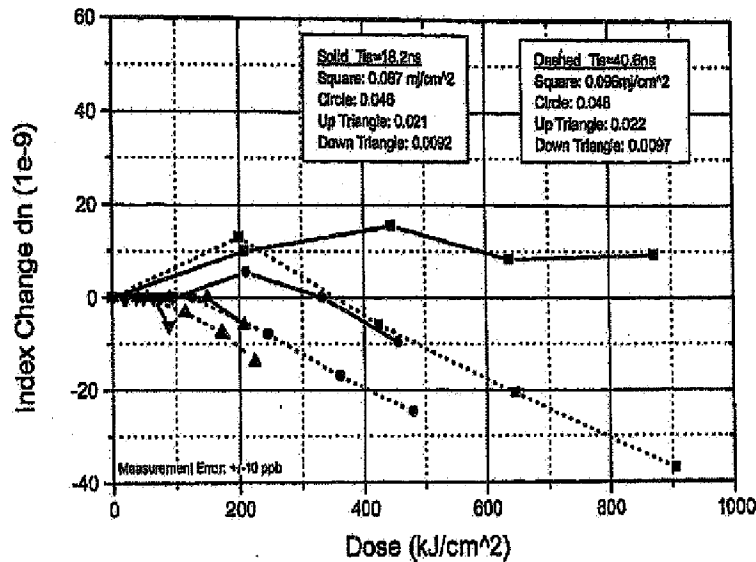


Figure 14 - Measured refractive index change for sample #3 with a good balance between compaction and rarefaction.

The results described above indicate that a combined model is required to describe the measured results for all these materials. Combining the compaction and rarefaction models gives the following:

$$\partial n = \Delta n_{sat} \left( 1 - e^{-\frac{N}{D_0}} \right) + \left( k_2 \frac{NI^2}{t_{fs}} \right)^b$$

In some cases the e-folding dose is so large that the rarefaction portion of the index change is better fit with a simple linear function. Sample #3 is one such case. Attempts at fitting to the exponential rarefaction model led to unrealistic values for the saturated index change and the e-folding value. The combination of the two values still led to a sensible initial slope, but instead we choose to model samples such as this with a simple linear rarefaction model combined with the compaction model:

$$\partial n = \frac{\Delta n_{sat}}{D_0} (NI) + \left( k_2 \frac{NI^2}{t_{fs}} \right)^b$$

where  $\frac{\Delta n_{sat}}{D_0}$  is the initial slope for the rarefaction index change.

We intend to continue exposing these samples until 40 billion pulses are accumulated. At the end of such long exposures, we expect that all samples will have exhibited saturation in the rarefaction component of refractive index change and thus we will be able to fit all samples to the full model.

Fitting the parameters of these combined models to the measured data for each of the samples gives the following results:

	<u>Sample #1</u>	<u>Sample #2</u>	<u>Sample #3*</u>
$\Delta n_{\text{sat}}$ (1e-9)	-23.4	-78.4	—
$D_0$ (kJ/cm <sup>2</sup> )	6168	279	—
Initial slope 1e-9-(kJ/cm <sup>2</sup> ) <sup>-1</sup>	-0.0038	-0.28	-0.11
$k_2 \left( \frac{\text{J}^2}{\text{cm}^4 \text{ ns}} \right)^{-1}$	1202	485	511
b (unitless)	0.53	0.61	0.60

\* Sample #3 was fit to the linear rarefaction model.

To demonstrate the accuracy of this combined model, Figure 15 shows the measured index change for sample #3 plotted against the index change predicted by the model. The close approximation to a straight line for this scatter plot, especially for both positive and negative refractive index change values, demonstrates the model's ability to predict measured performance.

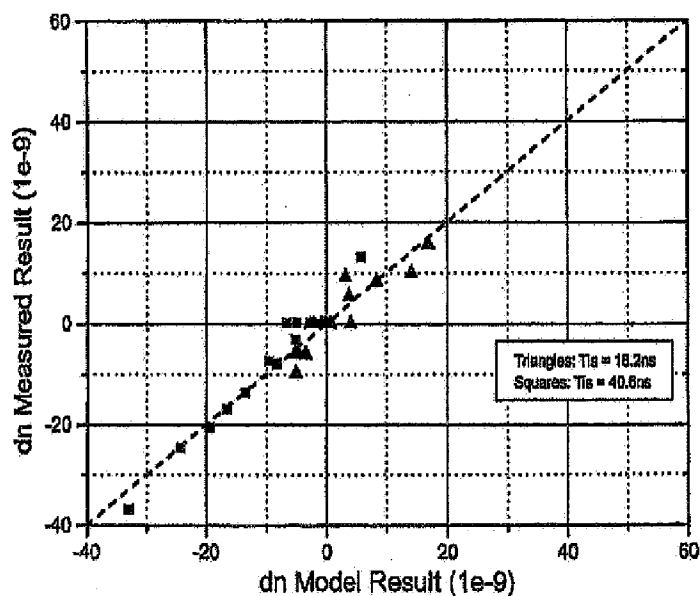


Figure 15 - Scatter plot comparing measured data for sample #3 against model prediction.

An interesting result occurs if we fix the  $b$  parameter to the value of 0.6 often quoted in prior work on compaction in fused silica exposed to high energy densities<sup>3</sup>. Fixing the  $b$  value is important for making a meaningful comparison between the  $k_2$  values<sup>7</sup> of different samples because small changes in  $b$  lead to large changes in  $k_2$ . With the  $b$  value fixed, the fitting results become:

	<u>Sample #1**</u>	<u>Sample #2</u>	<u>Sample #3*</u>
$\Delta n_{sat} (1e-9)$	0.0	-77.8	--
$D_0 (kJ/cm^2)$	--	273	--
Initial slope $1e-9 (kJ/cm^2)^{-1}$	0.0	-0.28	-0.11
$k_2 \left( \frac{J^2}{cm^4 ns} \right)^{-1}$	533	538	513
$b$ (fixed)	0.60	0.60	0.60

\* Sample #3 was fit to the linear rarefaction model.

\*\* The best fit for the saturated index change for sample #1 under these conditions is zero, thus there is no e-fold dose value.

With the  $b$  parameter fixed, the  $k_2$  values for all three samples become nearly the same, differing only 2.4% about an average value. We infer from this fitting result that all three samples have nearly the same compaction characteristics and it is the difference in rarefaction behavior that lead to the different refractive index changes found in these experiments.

## 5. Conclusions

Results of an experiment have been presented in which the parameters laser energy density, number of laser pulses, and pulse duration on the laser induced wavefront change in fused silica based on the modification of the optical index of refraction have been studied. Depending on the fused silica type different wavefront changes have been observed. Based on these results a combined model is developed that takes into account rarefaction and compaction effects and allows to predict the wavefront behavior. In addition, the effect of the pulse duration on laser induced wavefront deviations has been studied and taken into account in the model. Most essential result is that pulse stretching leads to less compaction effects in fused silica.

## References

1. J.E. Shelby, "Radiation Effects in Hydrogen-impregnated Vitreous Silica," J.Appl. Phys. 50, 3702 (1979).
2. C.M. Smith, N.F. Borrelli, J.J. Price, D.C. Allan, "Excimer Laser-induced Expansion in Hydrogen-loaded Silica," Appl. Phys. Lett. 78, 2452 (2001).
3. N.F. Borrelli, et al, "Densification of fused silica under 193nm excitation," J. Opt. Soc. Am. B 14, 1606-1615, 1997.

4. R. Sandstrom, *Proc of 2nd Symposium on 193nm Lithography*, Colorado Springs, CO, 1997.
5. R. Morton, et al, "Behavior of Fused Silica Materials for Microlithography Irradiated at 193nm with low-fluence ArF Radiation for tens of Billions of Pulses," *Proc SPIE 4000*, pp 496-510, 2000.
6. J. Moll and P. Dewa, "Laser Resistance of Fused Silica for Microlithography: Experiments and Models," *Proc SPIE 4691*, pp 1734-1741, 2002.
7. D.C. Allan, C. Smith, N.F. Borelli, "Measurement and Analysis of compaction in fused silica", *Symposium of Laser-Induced Damage in Optical Materials*, Boulder, Colorado, 1998, pp 16-27.